Ceramics International xxx (xxxx) xxx

Contents lists available at ScienceDirect

Ceramics International

journal homepage: www.elsevier.com/locate/ceramint

Direct Writing of SiC-polymer nanocomposites for humidity sensing with enhanced performance

Anasheh Khecho, Erina B. Joyee *

Mechanical Engineering and Engineering Science, University of North Carolina at Charlotte, Charlotte, NC, USA

ARTICLE INFO

Handling Editor: P. Vincenzini

Keywords:
Direct writing (DW)
Humidity sensors
Nanocomposite
Silicon carbide

ABSTRACT

Humidity sensors are essential for monitoring humidity levels in various fields. This paper investigates the development and optimization of humidity sensitive SiC-Fe_3O_4 polymer nanocomposites with varying Fe_3O_4 concentrations fabricated using Direct Writing (DW) process. The inks were evaluated for flow behavior to ensure proper extrudability through the nozzle. The rheological behavior was then correlated with the printing parameters to optimize the printing accuracy of the nanocomposites. It was observed that all the inks exhibited shear-thinning behavior, enabling a smooth extrusion process. To ensure high-resolution features, a new image analysis method was introduced to quantify corner rounding in printed features, enabling the optimization of printing parameters. In terms of humidity sensing performance, all the inks displayed a change in electrical properties with humidity adsorption. The fabricated nanocomposites showed a decrease in electrical conductivity with increasing humidity, suggesting potential for humidity-sensing applications. Notably, the humidity sensitivity of the nanocomposites was highly dependent on the Fe_3O_4 concentration in the inks. These findings provide valuable insights into the DW of SiC-Fe_3O_4 polymer nanocomposites for humidity sensing applications.

1. Introduction

Humidity sensors have become crucial devices for monitoring and controlling moisture levels across a diverse range of applications, from agriculture and meteorology to wearable technology and healthcare [1,2]. In healthcare, these sensors play an essential role in health monitoring systems by enabling rapid moisture detection through human respiration [3], sweating [4], or skin humidity [5]. The collected data from humidity sensors enables the early detection of urgent medical intervention, facilitates diagnosis, and provides personalized healthcare [6]. The growing demand for highly sensitive and responsive humidity sensors, particularly in wearable devices and human health monitoring systems, has motivated researchers to explore innovative materials and fabrication techniques [1,7].

Material selection is a pivotal factor in fabricating high-performance humidity sensors. These materials should exhibit responsivity to water molecules, minimal interference with non-water molecules, and high durability in absorption and desorption cycles [7,8]. Among different material options, ceramics offer several promising properties including high hardness, strength, and desirable electrical conductivity. They also possess excellent thermal and chemical stability, making them ideal candidates for humidity sensors specifically for harsh or extreme conditions. These properties ensure long-term reliability and position them as promising candidates for humidity sensors [9,10]. In ceramics, metal oxides are commonly used in conventional humidity sensors [7]. Perovskites such as Barium Titanate ($BaTiO_3$) [11,12] have shown promise due to their high dielectric constant and piezoelectric properties. Clay minerals such as montmorillonite [13] possess high surface area and can effectively absorb water molecules. Spinels like magnesium aluminate ($MgAl_2O_4$) [14,15] offer excellent thermal stability and humidity sensitivity. Additionally, reducing the particle size to the nanoscale can significantly enhance the performance of humidity sensors due to the increased surface area and improved reactivity [16,17]. Nanoparticles such as MWCNTs [17,18], TiO_2 [19], rGO [20], and Al_2O_3 [21,22], have been successfully used as primary sensing materials in humidity sensors.

On the other hand, semiconductor-based ceramic humidity sensors such as Silicon Carbide (SiC) have emerged as promising alternatives with faster responsivity and higher sensitivity to humidity due to different sensing mechanisms [10]. SiC is a wide band gap (2.4–3.2 eV) semiconductor with excellent thermal and chemical stability [23]. Li et al. [24] synthesized SiC nanopaper of long SiC nanowires and they found that the fabricated free-standing nanopaper showed a linear

* Corresponding author.
E-mail address: ejoyee@charlotte.edu (E.B. Joyee).

https://doi.org/10.1016/j.ceramint.2024.09.388
Received 9 August 2024; Received in revised form 20 September 2024; Accepted 28 September 2024
Available online 29 September 2024

relationship between relative humidity and electrical conductivity while creating a fast response and recovery times, proving its potential for susceptible humidity sensors. In another study, the synthesized SiC nanosheet pastes were coated onto Ag–Pd electrodes to fabricate a humidity sensor. The results showed that the developed sample was highly sensitive and fast responsive to moisture at a wide range of relative humidity levels demonstrating the superior properties of the sensor to the existing commercial options [25]. Even though past research has indicated the potential of SiC nanomaterials as semiconductor-based humidity sensors, the limited chemical reactivity of SiC with water still hinders its sensitivity as a humidity sensor, specifically in human health monitoring systems where the detection happens in trace amounts of moisture [26]. To address this issue, researchers have explored incorporating metal oxides such as ZnO [27], SnO_2 [28] to increase the number of active sites for water molecules' adsorption. However, despite the demonstrated potential, these materials have some limitations, such as poor mechanical flexibility, long response times, or challenges in large-scale manufacturing. This highlights the need for developing new composites, such as the SiC-Fe_3O_4-PVA nanocomposite presented in our study. Silicon carbide (SiC) offers significant advantages, including high thermal stability, chemical inertness, and the ability to form composites that overcome the shortcomings of traditional ceramic materials. We believe that further development of such composite materials can lead to more robust and efficient humidity sensing solutions.

To effectively use humidity sensors in wearable devices, varied flexibility is crucial. Combining ceramics with polymers, either as substrates or within the composite matrix, achieves the necessary flexibility for seamless integration into wearable systems [10]. This approach enhances the sensor's adaptability to the body's movements while maintaining its responsiveness to humidity changes, making it ideal for wearable applications [29].

While particle-polymer composites offer performance improvements, manufacturing devices with embedded sensors using traditional suspension-based fabrication techniques is challenging, often requiring multiple steps and extensive post-processing. These complexities make sensor integration difficult. However, advancements in Additive Manufacturing (AM), particularly Direct Writing (DW), have revolutionized the fabrication of multi-material sensors and soft electronics, providing a more efficient solution by enabling the direct printing of devices with embedded sensors in a single step, without the need for complex post-processing [30]. DW, an extrusion-based AM method offers greater design flexibility, cost-effectiveness, and the ability to create multi-component parts, making it an ideal technique for developing advanced devices. DW has gained significant attention due to its material versatility and simplicity. These attributes make DW particularly well-suited for fabricating multi-material systems that combine various filler particles and polymer matrices [31]. Numerous electronic systems, for instance, temperature, biochemical, humidity [32] and tactile [33] sensors for wearable devices and electronic skins have been successfully produced using the DW method.

However, the performance of such systems is directly tied to the precision of the printing process. Achieving high-quality, functional sensors requires careful material preparation and precise control of printing parameters to ensure optimal deposition and minimal defects. Printing accuracy is particularly critical in the case of humidity sensors, as it influences the structural integrity and surface morphology of the printed nanocomposite, both of which play crucial roles in sensor performance. Accurate deposition ensures uniform material distribution, leading to consistent interaction with environmental humidity and enhancing sensor sensitivity and response time. Furthermore, precise control over the printing process enables customization of the sensor's design for specific applications, providing advantages over commercially available, low-cost sensors in terms of adaptability and integration into complex geometries or wearable devices [34]. Ink rheology is another crucial factor in the DW process. For a continuous extrusion, non-Newtonian shear-thinning behavior is required. After extrusion, the viscoelastic properties of the ink help with the self-support and rapid shape recovery of the extrudate thus enabling the multilayer deposition of the ink [35,36]. Ensuring these conditions allows for the creation of high-performance humidity sensors with enhanced sensitivity and reliability. However, the extrusion and deposition process and the resulting printed structure are influenced by the DW process itself. Printing parameters such as nozzle inner diameter, flow rate, dispensing speed, and stand-off distance significantly impact the macrostructural properties and geometrical accuracy of the printed parts [37]. By accurately controlling these parameters, it is possible to regulate layer thickness, surface roughness, and trace dimensions, thereby optimizing sensor performance. The correlation of these two factors ensures accurate deposition of the ink, with minimal defects and high geometrical/dimensional accuracy [38].

One of the common challenges encountered in DW is the formation of corner defects that compromise dimensional accuracy and functional integrity. These defects deteriorate the sensor's performance by disrupting conductive pathways and hindering the sensor's fast response [39]. Jiang et al. [40] developed a normalized geometry prediction model to accurately predict the shape and size of printed traces in direct ink writing. They also identified the critical speed ratio for bulge-free printing, ensuring that the printed traces are free from defects. These advancements led to improved corner and sharp part accuracy in the direct ink writing process. In another study, Fredrich et al. [39] investigated corner defects in DW by studying the effects of support materials, corner geometries, and printing parameters on particle distribution. They found that corner swelling, ringing, and interfacial energy-driven smoothing contribute to these defects.

Our previous study was focused on investigating the rheological properties of the novel SiC-Fe_3O_4-polymer nanocomposite [41]. Building on that foundation, this work presents the extrusion-based fabrication and development of SiC-Fe_3O_4 nanocomposites, which show promise for applications in the humidity sensing industry. Understanding the critical relationship between flow behavior and printing accuracy, we employed a 2D acquisition technique to evaluate the corner accuracy of the printed traces and correlate it with the ink's performance in the Direct Writing (DW) process. Preliminary results indicate that the fabricated nanocomposites exhibit satisfactory sensitivity to humidity variations, demonstrating their potential for use in humidity sensing applications.

2. Experimental Procedure

2.1. Preparation of PVA substrate and SiC-Fe3O4 nanocomposite inks

The composite ink was prepared by mixing Polyvinyl alcohol polymer (PVA, Mw = 130,000, Sigma Aldrich, MI, USA), SiC nanopowder (Beta SiC, 99 %, <80 nm, cubic, US Nano, TX, USA) and magnetite powder (Fe_3O_4, >98 % purity, average diameter 300 nm, Alpha Chemicals, SEMO, USA). First PVA was dissolved in deionized water with a weight ratio of 15:100 to prepare a water-based polymeric solution. This solution was used as the ink for fabricating thin-film PVA substrates. Then the SiC nanoparticles and magnetite powder were dispersed in the polymeric solution and mechanically mixed until a homogeneous solution was obtained. The inks were loaded into a 5 mL syringe barrel and degassed in the centrifugal mixer for 5 min and at 400 rpm. Table 1 summarizes three different printing inks with varying

Table 1
Composition of the SiC-Fe_3O_4 composite inks.

Sample	SiC (wt %)	Fe_3O_4 (wt %)	PVA solution (wt %)	Total
5M	15	5	80	100
10M	15	10	75	100
15M	15	15	70	100

material compositions.

2.2. Experimental setup

In this study, the inks were 3D printed utilizing a robotic dispensing system (Nordson EFD, USA) similar to the setup described in our previous work [41]. This system was modified to function as a DW printer. The DW setup is illustrated in Fig. 1. The experimental setup includes a pressure controller to regulate the ink flow rate, a heat-controlled build platform, and a charge-coupled camera (CCD) camera. The platform temperature, controlled by the direct writing software, can be adjusted from −30 °C to 300 °C. Typically, an elevated temperature is used to evaporate moisture and solidify the printed trace quickly. The syringe tip was fixed to a Z stage, with the standoff distance adjusted according to the tip gauge for each experiment. The CCD camera was used to visually detect when the tip met the substrate and to monitor the dispensing process in real-time. To initiate a printing job, the stage was reset to the origin point. Upon reaching the starting position of a trace, the preprogrammed flow rate stopped at the end of the trace.

2.3. Rheological properties

To evaluate the suitability of the inks for the DW process, the flow behavior of the inks was evaluated using a Discovery HR-10 rheometer (TA Instruments, Inc. USA) with a 20 mm parallel plate geometry. The viscosity versus shear rate curves were obtained by performing a flow ramp test at room temperature in shear rates of 0.1–1000 s^{-1}. The parallel plate gap was set to 1 mm.

2.4. Fabrication process and image analysis

As illustrated in Fig. 1, the first step of the DW involves printing a four-layer 25 mm × 15 mm rectangle of PVA thin-film substrate on the fixed glass plate. To obtain a 150 μm thick PVA film, four layers of PVA polymeric ink with a layer height of 0.2 mm were deposited on the heated glass slide where it was fully dried in 5 min. After the formation of a PVA thin film as the substrate, the SiC-Fe_3O_4 nanocomposite inks were dispensed (extrusion air pressure of 48 kPa) on the PVA film based on an interdigitated CAD drawing (Fig. 1a) uploaded on the DW software.

The air pressures used for both PVA and SiC-Fe_3O_4 ink were determined based on the rheological properties of the materials, specifically their viscosities, and the corresponding flow rates. The flow rate Q is related to the applied air pressure P, material viscosity η, and the nozzle geometry, as described by a modified version of Hagen-Poiseuille's Law [42,43]:

$$Q \cong \frac{\pi r^4(P)}{8\eta L}$$

where r is the nozzle radius, P is the applied air pressure, η is the dynamic viscosity of the fluid, and L is the nozzle length. Given the higher viscosity of the SiC-Fe_3O_4 ink, an extrusion air pressure of 48 kPa was required to achieve the optimal flow rate, while a lower pressure of 30 kPa was sufficient for the less viscous PVA ink. These pressures were optimized through a series of experiments to ensure uniform and void-free deposition. Additionally, the nozzle geometry (410 μm inner diameter) and other printing parameters, such as build platform temperature (70 °C) and dispensing speeds, were chosen based on previous optimization studies [41].

The DW process parameters were evaluated by performing image analysis on the dried printed composites. First, the images were captured using Olympus (DSX1000) optical microscope. Then the images were analyzed using ImageJ software (Java 1.8.0_345) and by measuring the corners' incomplete and over-deposited material areas.

2.5. Humidity sensing performance

The humidity sensing performance was characterized by measuring the electrical resistance variation of the composites at room temperature (~25 °C) and in a controlled environment, with relative humidity (RH) levels ranging from 10 % to 100 %.

3. Results and discussion

3.1. Flow behavior

Determining the rheology behavior of the ink under steady and cyclic deformation modes provides valuable insight into the extrusion process and the fabrication of defect-free samples in DW. For the layer-by-layer DW process, the ink must exhibit non-Newtonian shear-thinning behavior. This rheological behavior ensures the effective extrudability of the ink through the tip. Following the extrusion process, the inks must have self-standing ability after dispensing [44,45]. In our previous work [41], the rheological properties of the SiC-Fe_3O_4-PVA inks were thoroughly studied and it was found that the addition of Fe_3O_4 particles to the SiC-PVA ink helped with the proper flow and viscoelasticity of the inks for DW process. Fig. 2a shows the viscosity versus the shear rate of the inks. It is observed that despite the varying magnetite particle concentrations, all the inks exhibit a shear-thinning behavior at all shear

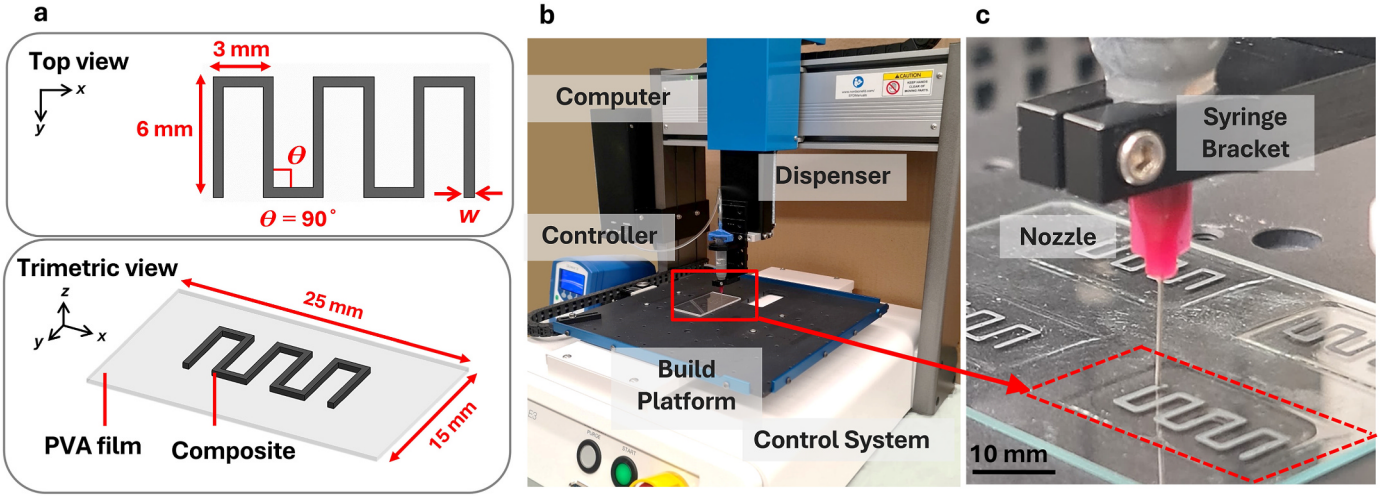

Fig. 1. a) CAD drawing of the humidity sensor; b) Direct Writing setup; c) Printed sample.

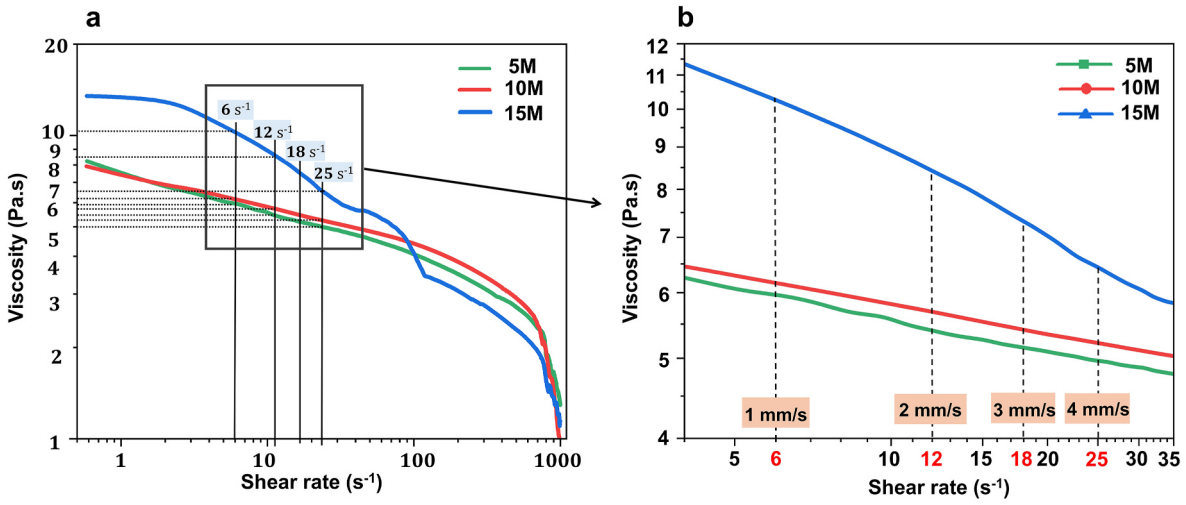

Fig. 2. a) Viscosity versus shear rate curves; b) Viscosity values at tip-induced shear rates.

rates, confirming the suitability of the inks for the extrusion process in DW. Consistently, the overall viscosity increases with higher magnetite particle loading. The higher solid loadings reduce inter-particle spaces, creating more interparticle bonds per volume and leaving less fluid to flow when sheared [46]. Despite the varying magnetite particle concentrations in 5M and 10M, the flow behavior follows similar plots with very close viscosity values. This suggests that regardless of higher solid content in 10 M, the larger size particles of Fe_3O_4 (<300 nm) have formed a polydisperse particle packing configuration where the interstitial nanoparticles among the larger particles provided the proper flow during the extrusion [35,47].

While ink flow behavior is crucial, other factors like nozzle diameter and dispensing speed also impact the DW process. These parameters affect printing accuracy and resolution. During the extrusion, a shear rate is induced at the nozzle tip that depends on the dispensing speed. This shear rate can be obtained by Equation (1), where $\dot{\gamma}$, Q, and r represent shear rate (s^{-1}), flow rate ($Q = s\,r^2$), and nozzle inner radius (mm), respectively and s is the dispensing speed [48,49].

$$\dot{\gamma} = \frac{4Q}{\pi r^3} \tag{1}$$

Correlating the ink flow behavior with DW printing parameters can help optimize the manufacturing process. Using Equation (1), the dispensing speeds were converted to tip-induced shear rates based on the used nozzle inner diameter (0.41 mm) and dispensing speeds of 1, 2, 3 and 4 mm/s. Then, the actual viscosity during the extrusion was identified by correlating the obtained shear rates with the flow behavior results.

Fig. 2b shows that the tip-induced shear rate changes from 6 to 25 s^{-1} as the dispensing speed increases from 1 to 4 mm/s. Considering the continuous viscosity drop of the inks with the shear rate increment, there is a reciprocal relation between the viscosity and dispensing speed. This means that the higher dispensing speed in shear-thinning fluids corresponds to a lower viscosity at the tip. Therefore, the DW printing parameters including dispensing speed can be readily altered to create the desired flowability at the tip of the nozzle. Proper flowability is an essential feature in the fabrication of sensors. Moreover, any micro- and macro-scale discontinuity in the nanocomposite structure can interrupt the sensing performance by creating a short circuit or false sensitivity of the part [50]. Therefore, introducing image analysis and printing accuracy inspection suggests a careful optimization process in DW. In the next section, the printing accuracy of the printed inks is discussed and correlated with the rheology results.

3.2. Image analysis

3.2.1. Theory

In this work, we studied how material and DW parameters affect the corner accuracy of the printed trace. We focused on dispensing speed and ink composition, as these factors influence corner accuracy through the ink's rheological behavior. Additionally, the non-viscoelastic nature of the inks allowed the elimination of the shape recovery after extrusion and obtaining a solidified composite layer through a heated build platform. Here, a preliminary image analysis method was developed to understand corner printing accuracy. The corner accuracy of the samples was studied by considering a divided structure where the corner area was isolated for more precise evaluation (Fig. 3a). The evaluations were assessed on the samples having 90-degree corners ($\Theta = 90°$).

To perform a 2-D acquisition of the corner geometry using optical microscopic images, samples were printed in a single-layer format to neglect the influence of thickness on the z-axis. Image analysis was then conducted on the pixelated areas (Fig. 3b) to quantify the rounding ratio in the corners compared to the intended printing pattern via ImageJ software. Rounding was attributed to the material overdeposition (R_{in_i}) in the inner corner and incomplete material deposition in the outer corner (R_{out_i}) relative to the total area of the intended line path. Equations (2) and (3) express roundness (RND) calculation methods developed in this work. For these calculations, the pixels are numbered according to the printing direction to simplify the process. For example, the subscript in R_{out_i} refers to the occupied area in pixel number i shown in Fig. 3c.

$$RND_{out} = \frac{Area\ of\ outer\ Corner}{Total\ area\ of\ the\ outer\ corner\ pixels} \tag{2}$$

$$RND_{in} = \frac{Area\ of\ inner\ Corner}{Total\ area\ of\ the\ inner\ corner\ pixels} \tag{3}$$

After determining in-charge corner pixels for each sample, the aforementioned equations were elaborated considering the summation of the occupied area in each pixel (R_{out_i}) and the total pixels' number (n) leading to equations (4) and (5). W_1 and W_2 are printed line widths in the x and y directions, respectively. The total area of the pixels was determined based on the printed line width in the x and y directions as shown in Fig. 3c.

$$RND_{out} = \frac{\sum R_{out_i}}{n \times \left(\frac{1}{4}\, W_1\ \ W_2\right)} \tag{4}$$

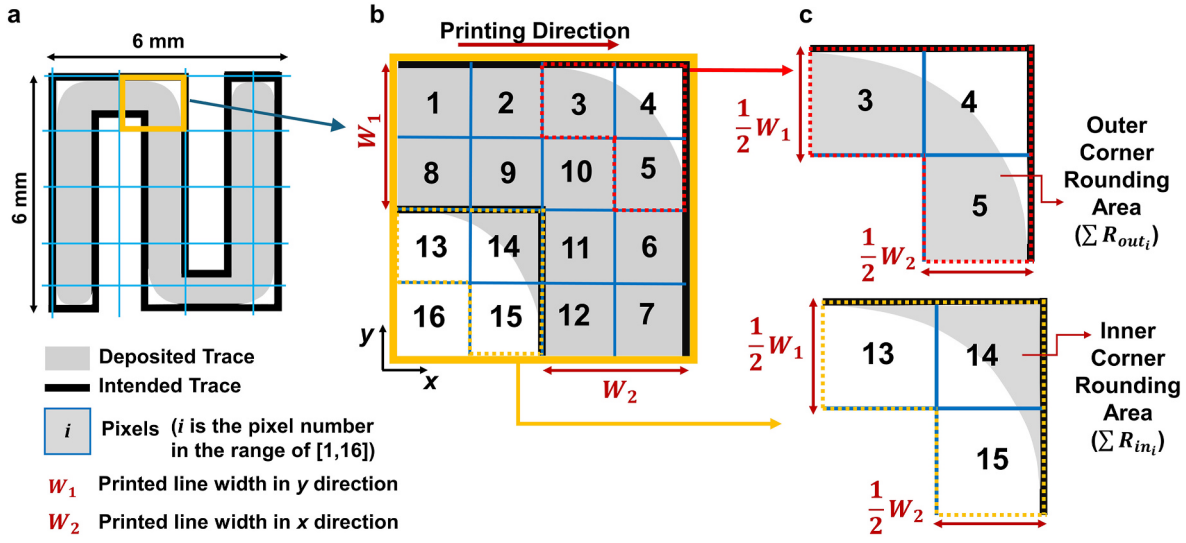

Fig. 3. Accuracy evaluation method; a) Schematic of the actual printed pattern; b) Pixelated area of the corner; c) Inner and outer corner rounding.

$$RND_{in} = \frac{\sum R_{in_i}}{n \times \left(\frac{1}{4} W_1 W_2\right)} \tag{5}$$

After obtaining the roundness percentages in each sample, the printing parameters optimization was performed. Acceptable accuracy levels were defined as a minimum of 80 % for the outer and a maximum of 25 % for the inner corner. The best parameters were identified by calculating the ρ ratio in Equation (6). A ρ value equal to or greater than 3 ($\rho \geq 3.2$) indicates acceptable accuracy in each sample. This ratio represents a dimensionless value that is independent of the nozzle diameter (D) and the pixel shape, making this method applicable to non-perpendicular corners ($\Theta \neq 0$).

$$\frac{RND_{out}}{RND_{in}} = \frac{\sum R_{OUT_i}}{\sum R_{IN_i}} = \rho \tag{6}$$

3.2.2. Corner accuracy evaluation

Fig. 4 illustrates the inner and outer corner accuracy results based on equations (3) and (4). It was observed that changing the dispensing speed from 1 to 4 mm/s affected the accuracy differently in each ink. This is because of the varying magnetite concentration that consequently created different flow behavior. Notably, at a dispensing speed of 1 mm/s, the outer corner roundness falls between ~82 and 84 %. This suggests that the 1 mm/s speed created the proper flow rate for depositing an adequate amount of ink regardless of the different rheological behaviors (Fig. 3). At 2 mm/s, the 5M and 10M samples have similar roundness percentages (82.90 ± 0.7 and 80.17 ± 0.1), whereas the value drops significantly in 15M (72.99 ± 3.2 %), resulting in poor outer corner accuracy. At 3 mm/s dispensing speed, there is an increasing accuracy in the outer corner from 5M to 15M. The trend changes when the speed increases to 4 mm/s making it the fastest flow rate amongst samples. Outer corner roundness increases from 63.79 ± 3.5 in the 5M sample to 83.03 ± 0.7 % in the 10M sample, then slightly decreases to 80.58 ± 1.1 % in 15M sample.

In contrast to outer corners, inner corner roundness percentages follow a distinct trend. For the 5M ink, the roundness decreases drastically from 37.13 ± 0.6 to 6.35 ± 0.86 (3 mm/s) and then rises to 13.31 ± 1.3 suggesting that a speed range of 2–3 mm/s is more suitable for achieving acceptable inner corner accuracy.

The 10M sample (containing 10 wt% magnetite particles) exhibits less sensitivity to flow rate changes within the tested range (1–4 mm/s), with inner corner roundness percentages remaining between 8 and 9.6 %. However, the 15M sample displays a declining trend similar to 5M, decreasing from 43.03 ± 3.4 % to 9.20 ± 0.2 % as the speed increases to 4 mm/s. Therefore, this indicates that in 15M the faster dispensing speeds enable more accurate ink deposition.

Overall, the outer and inner corners results follow a second-order polynomial model found by fitting the data. This indicates a correlation between dispensing speed and the accuracy of the samples. By establishing a relationship between the printing parameters and the resulting accuracy, we can optimize the dispensing process to achieve more consistent and reliable results, leading to enhanced quality and efficiency in the DW process.

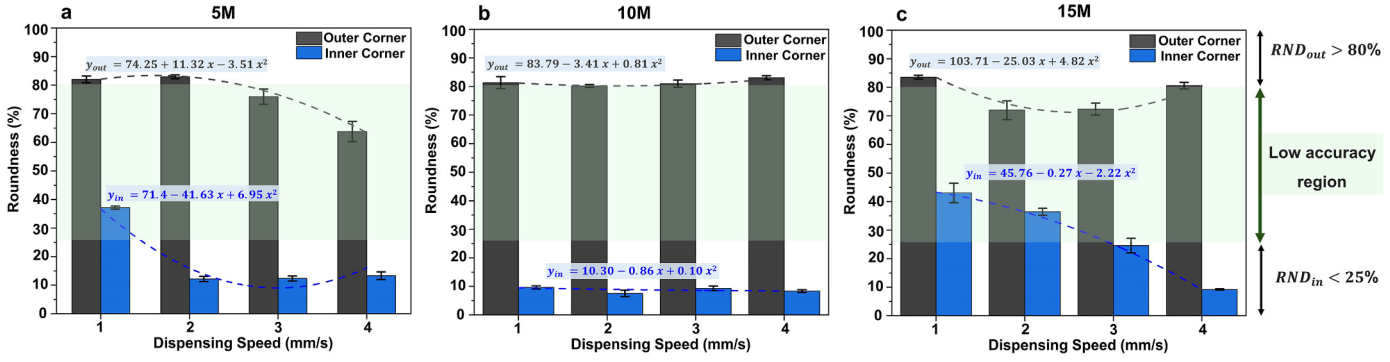

Fig. 4. Outer and inner rounding percentages versus dispensing speed and magnetite particle concentrations: a) 5M; b) 10M; c) 15M. (y_{in} and y_{out} denote the polynomial equations fitted to the data.)

3.2.3. Printing accuracy versus flow behavior

Even though the DW process is known for its versatility and uncomplicated working principle, obtaining smooth and optimized process parameters requires extended trials and errors. While the image analysis and corner accuracy evaluation results provide valuable insights into achieving optimal corner accuracy for different ink compositions, they can also lead to complex optimization processes. Thus, evaluating the instantaneous rheological behavior and the printing process becomes essentially important for predicting printing accuracy [34]. These printing parameters mainly include extrusion pressure, nozzle shape, internal diameter, and dispensing speed [51]. One of the key parameters affecting printing accuracy is the dispensing speed. This is because the extrusion process is accompanied by a complicated flow mechanism on a microscale and the dispensing speed directly manipulates the flow rate [52]. Generally, in fluids with low elastic modulus, the printing accuracy can be altered more easily when the dispensing speed is higher. However, there is no defined model that explains the relationship among dispensing speed, printing accuracy, and flow behavior for each fluid. To address this gap, we established an approach for optimizing printing parameters based on the ρ ratio calculated using Equation (5).

Fig. 5 presents a correlative comparison of the printing accuracy (ρ), and printing viscosity obtained from the image analysis and flow behavior results. The ρ ratio combines the roundness values in the outer and inner corners into a single value. Based on the defined minimum and maximum limits for accuracy, the ρ ratio is categorized into three groups: low ($\rho < 3.2$), acceptable ($3.2 < \rho < 8$), and high ($\rho > 8$) accuracy regions. Higher ρ values suggest high roundedness in the outer and low roundness in the inner corner, signifying a more desirable printing outcome. For instance, the 15M sample printed at a speed of 4 mm/s was identified as a favorable printed corner amongst other speeds with a ρ value of ~8.75 in the high-accuracy region. This analysis is also applicable to the different samples. 5M-2s, 10M-4s, and 15M-4s are the best-printed parts among the 12 samples.

It can be seen in Fig. 5 that 5M and 10M inks have completely different results despite the close viscosity ranges. This highlights the sensitivity of the DW process to the process parameters and flow mechanisms. In 5M, the accuracy ratio rises to ~7 at 2 mm/s speed and then significantly drops to ~2 as the speed decreases to 1 mm/s and the printing viscosity reaches ~6 Pa s. This rise suggests that the dispensing speed range of higher than 2 mm/s created low printing viscosity at the tip and caused more incomplete material deposition at the outer corner.

This can be ascribed to the interplay between the flow rate and the shear-thinning rheology of the ink. At lower speeds (1 mm/s), the higher tip viscosity allows better deposition of the ink. However, at higher speeds (2–4 mm/s), the increased shear forces within the ink might lead to lower viscosity during extrusion. This causes the ink to flow past the sharp inner corner instead of depositing adequately leading to decreased roundness.

The accuracy level decrease is also observed in 10M where the ρ value changes from 10 to 8.5 with the viscosity increment. This behavior could be due to the 10M ink's potentially higher viscosity or shear thinning properties. These properties might allow the ink to resist the shear forces better at higher speeds. This enables better filling of the inner corner geometry compared to the 5M ink. However, in 15M the accuracy shows a drastic deterioration when the dispensing speed reaches its quarter value. Considering the increase in viscosity with the decreased dispensing speed, it appears that regardless of the lower printing viscosity, it was easier to control the accuracy level at higher speeds. While the 15M ink might have a higher viscosity than 5M, potentially leading to some improvement in inner corner filling at lower speeds, it is limited by its flow characteristics at higher speeds.

While material selection is a fundamental factor in determining humidity sensing performance, other factors such as structural design and the surface area of the sensing layer also significantly influence overall sensitivity. Utilizing AM, particularly DW, allows for the fabrication of geometrically complex designs with optimized surface areas, enhancing the surface reactivity of the nanocomposites. To ensure optimal humidity sensing performance, it is essential to precisely characterize the printing accuracy of the nanocomposite material. By optimizing key printing parameters, such as dispensing speed, nozzle size, and ink composition, a more uniform and defect free print line structure was achieved. This improvement in printing resolution and quality directly enhances sensor performance by ensuring material uniformity and consistency, reducing defects, and maximizing the surface area available for water absorption. In the following section, the samples with the highest printing accuracy for each composition were tested for their humidity sensing capabilities.

3.3. Humidity sensing

The electrical properties of the nanomaterials can be readily altered by controlling the adsorption of gas molecules, including water molecules on the surface [24]. In this study, the humidity sensing performance of the nanocomposites was evaluated based on the change in electrical resistance shown in Equation (7). The S value represents the humidity sensitivity and R_h and R_0 are the nanocomposite's electrical resistance values at 10 % and other relative humidity (RH) levels, respectively.

$$S = \frac{R_h - R_0}{R_0} \tag{7}$$

Fig. 6 shows the humidity test setup, the fully integrated 3D printed nanocomposite, and the corresponding humidity sensing performance results. To understand the feasibility and comfort of the printed nanocomposite for potential applications in electronic skin and wearable devices, the nanocomposite was attached to human skin and its flexibility was tested. The change in resistance and humidity sensitivity

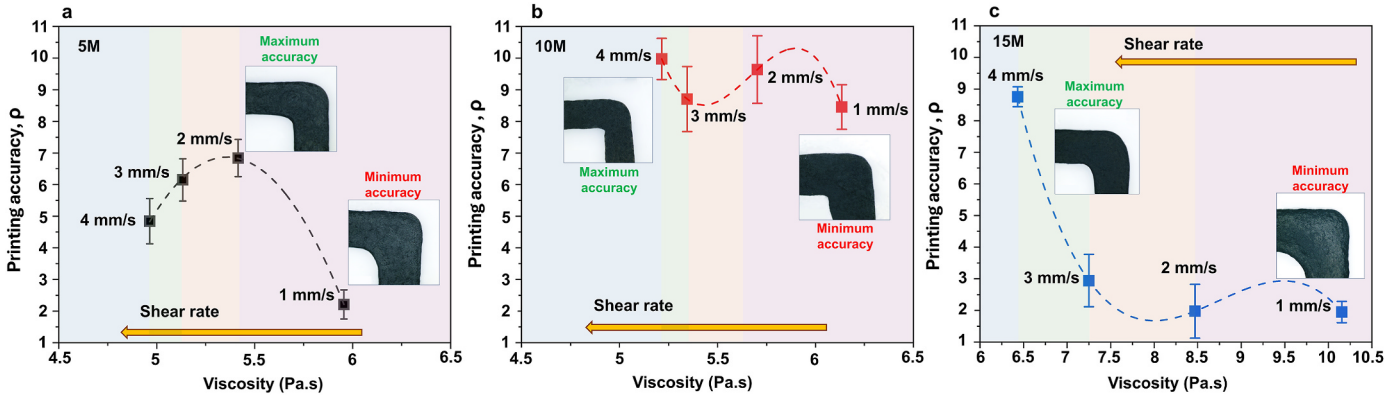

Fig. 5. Calculated ρ value versus printing viscosity: a) 5M ink; b)10M ink; c) 15M ink.

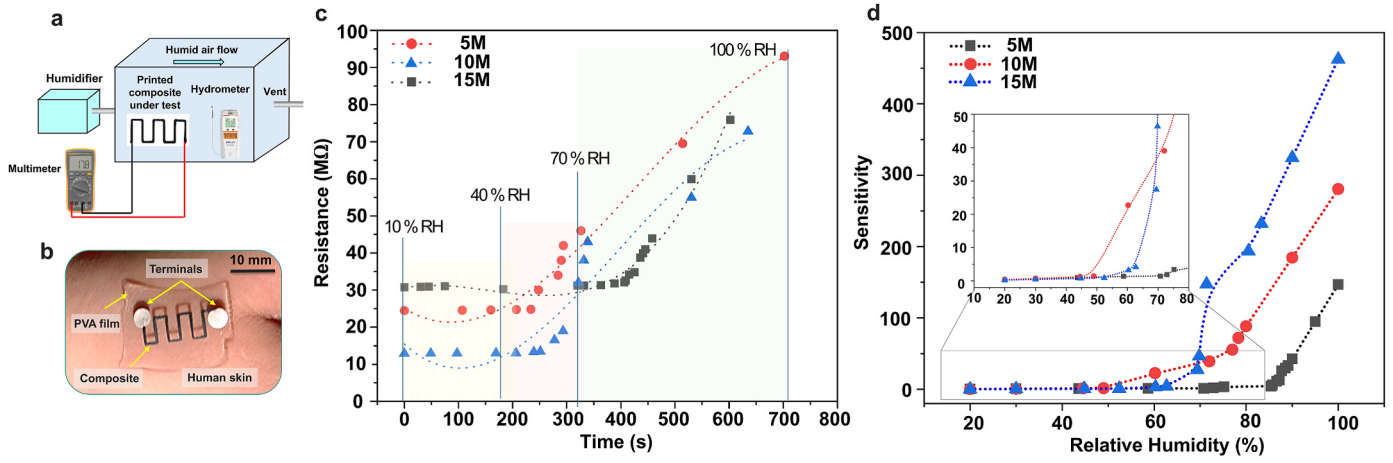

Fig. 6. a) Block diagram of humidity sensing test setup. b) A fully integrated 3D printed humidity sensor attached to human skin; c) Resistance change of the nanocomposite in under varying relative humidity; d) Humidity sensitivity of the nanocomposites in different relative humidity levels.

changes are recorded in different 3D printed nanocomposites with varying Fe_3O_4 concentrations at indoor relative humidity ranging from 10 to 100 %. It was observed that the adsorption of water molecules on the surface influenced the electrical conductivity of the SiC-based nanocomposite (Fig. 6c). Adsorption of water molecules is often accompanied by an increase in conductivity, mainly due to the higher electron/ion mobility [1,53]. However, based on the obtained values, a different sensing mechanism is observed in the SiC-Fe_3O_4-PVA nanocomposites. As seen in Fig. 6d, the nanocomposite exhibits higher sensitivity corresponding to the decrease in electrical conductivity. This is associated with the intrinsic semiconductivity of SiC and Fe_3O_4 particles and the insulating nature of the PVA polymeric matrix in the nanocomposite. Although SiC nanoparticles have the highest conductivity among other components in this system, the combination of the lesser semiconductive Fe_3O_4 particles and insulator PVA chains results in reduced electron mobility upon the absorbance of water molecules. Furthermore, the hygroscopicity of the PVA polymer accelerates the water adsorption by forming hydrogen bonds with water molecules. Simultaneously, the presence of water molecules in hydrophilic PVA chains causes microscale swelling in the nanocomposite. The swelling interrupts the conductive paths for water molecules' electron transfer, leading to a reduced number of conductive charge carriers, and consequently a substantial rise in the resistance [29,54].

The nanocomposites demonstrate less sensitivity in a dry atmosphere (10–40 % RH) whereas the sensitivity rises rapidly as the relative humidity level increases reaching a maximum of 463 in 15M. This can be attributed to the formation of different water molecule layers on the surface during the adsorption. In lower RH levels, the adsorption occurs through the chemisorption of water molecules by forming hydrogen bonding on the surface of the particles and the PVA chains. The hydrogen bonding is also formed through the thin nanometric layer of SiO_2 present on the surface of SiC nanoparticles and the hydroxyl groups on Fe_3O_4 particles. Therefore, the change in the conductivity becomes more prominent as the RH increases and the adsorption process is elevated to physisorption. In this step, the water molecules are only deposited on top of the chemisorbed layer forming multiple layers of water molecules on the surface [14,40].

Additionally, the humidity sensitivity of the nanocomposites is influenced by the concentration of the Fe_3O_4 particles. The addition of Fe_3O_4 particles boosted the humidity sensing properties of SiC-based nanocomposite. In the arid atmospheres (RH< 40 %), no humidity detection is observed in all samples whereas the moisture detection begins in 10M and 15M nanocomposites as the RH level passes 40 % and 50 %, respectively. 5M nanocomposite does not exhibit humidity detection until 85 % RH, making this composition unsuitable for humidity sensing purposes. Moreover, in 10M and 15M nanocomposites, the sensitivity grows exponentially up to the values of 300 and 436 in a humid and saturated atmosphere. The effect of Fe_3O_4 in enhanced humidity sensing performance can be ascribed to the reverse spinel crystal structure of this metal oxide. It is found that materials with spinel crystal structures provide active sites for water molecule deposition, making it easier to trap the water molecules and measure the electrical properties variations [1,55]. Overall, higher amounts of Fe_3O_4 particles created high sensitivity but at the same time lowered the humidity sensing range.

While this study primarily focused on the effects of humidity on the nanocomposite's electrical conductivity, it is also important to consider the potential impact of environmental temperature. Temperature can influence both water molecule adsorption and the overall conductivity of nanocomposites [56]. Due to the thermoelectric properties of SiC, elevated temperatures (~500 °C) could lead to impurity ionization, which may enhance electrical conductivity and improve humidity detection. However, the high purity of the SiC nanoparticles used in this composite (99.5 %) may mitigate the effects of temperature variations specifically at low temperatures (25–100 °C), resulting in minimal or negligible increases in conductivity [57]. In contrast, for Fe_3O_4, the increased ion mobility at higher temperatures due to increased ion mobility, can enhance both electrical conductivity and water absorption [58]. Similarly, PVA is known to absorb more water at higher temperatures [59], suggesting that the developed nanocomposite may exhibit temperature-dependent humidity sensitivity within specific temperature ranges.

Future research should explore the combined effects of temperature and environmental conditions on the sensing performance of these nanocomposites. Although further investigations are required to optimize the humidity-sensing capabilities, these findings indicate that SiC-Fe_3O_4-PVA nanocomposites hold promise for humidity-sensing applications.

4. Conclusions

In conclusion, we successfully developed SiC-Fe_3O_4 nanocomposite humidity-sensitive parts using a (DW) AM technique. The ink processability was evaluated and the prepared ink exhibited shear-thinning behavior, making it suitable for extrusion through a nozzle. By correlating the rheological properties with the printing parameters, we were able to optimize the printing accuracy. The image analysis method developed in this work allowed for the quantification of corner rounding

in the printed patterns and identified the optimal printing parameters for high resolution and dimensional accuracy fabrication of parts. The electrical properties of the DW-printed nanocomposites were investigated for humidity-sensing applications. The nanocomposites exhibited a decrease in electrical conductivity with increasing relative humidity, suggesting a promising potential for humidity sensor applications. Future work will focus on further optimizing the humidity sensing performance of the nanocomposites by exploring different material compositions and printing parameters.

Funding

This research was funded by National Science Foundation, Directorate for Engineering (Award ID: 2301462)

CRediT authorship contribution statement

Anasheh Khecho: Writing – original draft, Validation, Methodology, Data curation, Conceptualization. **Erina B. Joyee:** Writing – review & editing, Writing – original draft, Validation, Supervision, Resources, Methodology, Investigation, Funding acquisition, Conceptualization.

Declaration of competing interest

The authors declare that they have no competing financial interests or personal relationships that could have appeared to influence the work reported in this paper.

Acknowledgments

No competing financial interests exist for any author.

References

[1] T.A. Blank, L.P. Eksperiandova, K.N. Belikov, Recent trends of ceramic humidity sensors development: a review, Sens Actuators B Chem 228 (2016) 416–442, https://doi.org/10.1016/j.snb.2016.01.015.

[2] M.V. Kulkarni, S.K. Apte, S.D. Naik, J.D. Ambekar, B.B. Kale, Ink-jet printed conducting polyaniline based flexible humidity sensor, Sens Actuators B Chem 178 (2013) 140–143, https://doi.org/10.1016/j.snb.2012.12.046.

[3] L. Ma, R. Wu, A. Patil, S. Zhu, Z. Meng, H. Meng, C. Hou, Y. Zhang, Q. Liu, R. Yu, J. Wang, N. Lin, X.Y. Liu, Full-textile wireless flexible humidity sensor for human physiological monitoring, Adv. Funct. Mater. 29 (2019), https://doi.org/10.1002/adfm.201904549.

[4] B. Zhong, K. Jiang, L. Wang, G. Shen, Wearable sweat loss measuring devices: from the role of sweat loss to advanced mechanisms and designs, Adv. Sci. 9 (2022), https://doi.org/10.1002/advs.202103257.

[5] W. Jeong, J. Song, J. Bae, K.R. Nandanapalli, S. Lee, Breathable nanomesh humidity sensor for real-time skin humidity monitoring, ACS Appl. Mater. Interfaces (2019), https://doi.org/10.1021/acsami.9b17584.

[6] Y. Hou, M. Gao, J. Gao, L. Zhao, E.H.T. Teo, D. Wang, H.J. Qi, K. Zhou, 3D printed conformal strain and humidity sensors for human motion prediction and health monitoring via machine learning, Adv. Sci. 10 (2023) 1–13, https://doi.org/10.1002/advs.202304132.

[7] B. Arman Kuzubasoglu, Recent studies on the humidity sensor: a mini review, ACS Appl. Electron. Mater. 4 (2022) 4797–4807, https://doi.org/10.1021/acsaelm.2c00721.

[8] D. Barmpakos, G. Kaltsas, A review on humidity, temperature and strain printed sensors—current trends and future perspectives, Sensors 21 (2021) 1–24, https://doi.org/10.3390/s21030739.

[9] N.V. Krishna Prasad, K. Venkata Prasad, S. Ramesh, S.V. Phanidhar, K. Venkata Ratnam, S. Janardhan, H. Manjunatha, M.S.S.R.K.N. Sarma, K. Srinivas, Ceramic Sensors: a mini-review of their applications, Front Mater 7 (2020) 1–11, https://doi.org/10.3389/fmats.2020.593342.

[10] C.A. Ku, C.K. Chung, Advances in humidity nanosensors and their application: review, Sensors 23 (2023), https://doi.org/10.3390/s23042328.

[11] J. Yuk, T. Troczynski, Sol-gel BaTiO3 thin film for humidity sensors, Sens Actuators B Chem 94 (2003) 290–293, https://doi.org/10.1016/S0925-4005(03)00371-X.

[12] J. Wang, B. Xu, G. Liu, J. Zhang, T. Zhang, Improvement of nanocrystalline BaTiO humidity sensing properties. www.elsevier.nlrlocatersensorb, 2000.

[13] P.G. Su, C.Y. Chen, Humidity sensing and electrical properties of Na- and K-montmorillonite, Sens Actuators B Chem 129 (2008) 380–385, https://doi.org/10.1016/j.snb.2007.08.032.

[14] P. Misra, R.K. Shukla, L.M. Bali, C.L. Gupta, G.C. Dubey, EPR studies of some thick film ferrates, aluminates and their correlation with humidity sensitivity, Sens Actuators B Chem 94 (2003) 210–215, https://doi.org/10.1016/S0925-4005(03)00346-0.

[15] K. Ahn, B.W. Wessels, S. Sampath, Spinel humidity sensors prepared by thermal spray direct writing, in: Sens Actuators B Chem, Elsevier, 2005, pp. 342–346, https://doi.org/10.1016/j.snb.2004.10.020.

[16] G.Y. Li, J. Ma, G. Peng, W. Chen, Z.Y. Chu, Y.H. Li, T.J. Hu, X.D. Li, Room-temperature humidity-sensing performance of SiC nanopaper, ACS Appl. Mater. Interfaces 6 (2014) 22673–22679, https://doi.org/10.1021/am5067496.

[17] R. Aman Qazi, M. Saleem Khan, M. Siddiq, R. Ullah, L. Ali Shah, M. Ali, Synthesis and characterization of functionalized MWCNTs/PMMA composites: device fabrication for RH sensing, Polymer-Plastics Technology and Materials 59 (2020) 1608–1620, https://doi.org/10.1080/25740881.2020.1759631.

[18] C. Cai, W. Zhao, J. Yang, L. Zhang, Sensitive and flexible humidity sensor based on sodium hyaluronate/MWCNTs composite film, Cellulose 28 (2021) 6361–6371, https://doi.org/10.1007/s10570-021-03926-3.

[19] S. Atalay, T. Izgi, V.S. Kolat, S. Erdemoglu, O.O. Inan, Magnetoelastic humidity sensors with TiO2 nanotube sensing layers, Sensors 20 (2020), https://doi.org/10.3390/s20020425.

[20] C. Lei, J. Zhang, T. Liang, R. Liu, Z. Zhao, J. Xiong, K. Yin, Humidity sensor based on rGO-SDS composite film, Micromachines 13 (2022), https://doi.org/10.3390/mi13040504.

[21] B. Cheng, B. Tian, C. Xie, Y. Xiao, S. Lei, Highly sensitive humidity sensor based on amorphous Al2O 3 nanotubes, J. Mater. Chem. 21 (2011) 1907–1912, https://doi.org/10.1039/c0jm02753g.

[22] G. Sberveglieri, R. Anchisini, R. Murri, C. Ercoli, N. Pinto, An Al2O3 Sensor for Low Humidity Content: Characterization by Impedance Spectroscopy, 1996.

[23] H.Y. Wang, Y.Q. Wang, Q.F. Hu, X.J. Li, Capacitive humidity sensing properties of SiC nanowires grown on silicon nanoporous pillar array, Sens Actuators B Chem 166–167 (2012) 451–456, https://doi.org/10.1016/j.snb.2012.02.087.

[24] G.Y. Li, J. Ma, G. Peng, W. Chen, Z.Y. Chu, Y.H. Li, T.J. Hu, X.D. Li, Room-temperature humidity-sensing performance of SiC nanopaper, ACS Appl. Mater. Interfaces 6 (2014) 22673–22679, https://doi.org/10.1021/am5067496.

[25] L. Sun, B. Wang, Y. Wang, A novel silicon carbide nanosheet for high-performance humidity sensor, Adv Mater Interfaces 5 (2018) 1–9, https://doi.org/10.1002/admi.201701300.

[26] K. Sun, T. Wang, W. Gong, W. Lu, X. He, E.G. Eddings, M. Fan, Synthesis and potential applications of silicon carbide nanomaterials/nanocomposites, Ceram. Int. 48 (2022) 32571–32587, https://doi.org/10.1016/j.ceramint.2022.07.204.

[27] V.B. Platonov, M.N. Rumyantseva, A.S. Frolov, A.D. Yapryntsev, A.M. Gaskov, High-temperature resistive gas sensors based on ZnO/SiC nanocomposites, Beilstein J. Nanotechnol. 10 (2019) 1537–1547, https://doi.org/10.3762/bjnano.10.151.

[28] B. Wang, Y. Wang, Y. Lei, S. Xie, N. Wu, Y. Gou, C. Han, Q. Shi, D. Fang, Vertical SnO2 nanosheet@SiC nanofibers with hierarchical architecture for high-performance gas sensors, J Mater Chem C Mater 4 (2016) 295–304, https://doi.org/10.1039/c5tc02792f.

[29] W. Ahmad, B. Jabbar, I. Ahmad, B.M. Jan, M.M. Stylianakis, G. Kenanakis, R. Ikram, Highly sensitive humidity sensors based on polyethylene oxide/cuo/multi walled carbon nanotubes composite nanofibers, Materials 14 (2021) 1–19, https://doi.org/10.3390/ma14041037.

[30] A. Khecho, E.B. Joyee, Design and fabrication of bioinspired pattern driven magnetic actuators, Functional Composites and Structures 6 (2024), https://doi.org/10.1088/2631-6331/ad335f.

[31] S.D. Lacey, D.J. Kirsch, Y. Li, J.T. Morgenstern, B.C. Zarket, Y. Yao, J. Dai, L. Q. Garcia, B. Liu, T. Gao, S. Xu, S.R. Raghavan, J.W. Connell, Y. Lin, L. Hu, Extrusion-based 3D printing of hierarchically porous advanced battery electrodes, Adv. Mater. 30 (12) (2018) 17056651.

[32] R.Y. Tay, Y. Song, D.R. Yao, W. Gao, Direct-ink-writing 3D-printed bioelectronics, Mater. Today 71 (2023) 135–151, https://doi.org/10.1016/j.mattod.2023.09.006.

[33] X. Zhang, H. Hu, D. Tang, C. Zhang, J. Fu, P. Zhao, Magnetic flexible tactile sensor via direct ink writing, Sens Actuators A Phys 327 (2021), https://doi.org/10.1016/j.sna.2021.112753.

[34] B. Liu, Y. Zhao, Y. Li, L. Tao, P. Pan, Y. Bi, S. Song, L. Yu, Investigation of the structure, rheology and 3D printing characteristics of corn starch regulated by glycyrrhizic acid, Int. J. Biol. Macromol. 263 (2024), https://doi.org/10.1016/j.ijbiomac.2024.130277.

[35] P. Wei, C. Cipriani, C.M. Hsieh, K. Kamani, S. Rogers, E. Pentzer, Go with the flow: rheological requirements for direct ink write printability, J. Appl. Phys. 134 (2023), https://doi.org/10.1063/5.0155896.

[36] L. del-Mazo-Barbara, M.P. Ginebra, Rheological characterisation of ceramic inks for 3D direct ink writing: a review, J. Eur. Ceram. Soc. 41 (2021) 18–33, https://doi.org/10.1016/j.jeurceramsoc.2021.08.031.

[37] B.C. Palivela, S.D. Bandari, R.S. Mamilla, Extrusion-based 3D printing of bioactive glass scaffolds-process parameters and mechanical properties: a review, Bioprinting 27 (2022) e00219, https://doi.org/10.1016/j.bprint.2022.e00219.

[38] S. Lamnini, H. Elsayed, Y. Lakhdar, F. Baino, F. Smeacetto, E. Bernardo, Robocasting of advanced ceramics: ink optimization and protocol to predict the printing parameters - a review, Heliyon 8 (2022) e10651, https://doi.org/10.1016/j.heliyon.2022.e10651.

[39] L. Friedrich, M. Begley, Corner accuracy in direct ink writing with support material, Bioprinting 19 (2020), https://doi.org/10.1016/j.bprint.2020.e00086.

[40] Y. Jiang, S. Hu, Y. Pan, A normalized trace geometry modeling method with bulge-free analysis for direct ink writing process planning, 3D Print. Addit. Manuf. 5 (2018) 301–310, https://doi.org/10.1089/3dp.2017.0132.

[41] A. Khecho, R. Hewlin, E.B. Joyee, Direct ink writing of SiC-Fe3O4-polymer nanocomposites for magnetic humidity sensors: rheology characterization, in:

International Manufacturing Science and Engineering Conference, American Society of Mechanical Engineers, 2024, https://doi.org/10.1115/MSEC2024-124489.

[42] B.C. Eu, Generalization of the Hagen–Poiseuille velocity profile to non-Newtonian fluids and measurement of their viscosity, Am. J. Phys. 58 (1990) 83–84, https://doi.org/10.1119/1.16328.

[43] S.P. Sutera, R. Skalak, THE HISTORY OF POISEUILLE'S LAW, n.d. www.annualreviews.org.

[44] Y. Liu, C. Chen, L. Liu, G. Zhu, Q. Kong, R. Hao, W. Tan, Rheological behavior of high concentrated dispersions of graphite oxide, Soft Mater. 13 (2015) 167–175, https://doi.org/10.1080/1539445X.2015.1055004.

[45] A. Khecho, S.A. Ghaffari, B. Eftekhari Yekta, The influence of particle size distribution on rheological properties of fused silica pastes for direct ink writing, Int. J. Appl. Ceram. Technol. 19 (2022) 2472–2479.

[46] S.S.L. Chan, R.M. Pennings, L. Edwards, G.V. Franks, 3D printing of clay for decorative architectural applications: effect of solids volume fraction on rheology and printability, Addit. Manuf. 35 (2020) 101335, https://doi.org/10.1016/j.addma.2020.101335.

[47] Z.C. Chen, K. Ikeda, T. Murakami, T. Takeda, Effect of particle packing on extrusion behavior of pastes, J. Mater. Sci. 35 (2000) 5301–5307, https://doi.org/10.1023/A:1004834526344.

[48] A. M'Barki, L. Bocquet, A. Stevenson, Linking rheology and printability for dense and strong ceramics by direct ink writing, Sci. Rep. 7 (2017) 1–10, https://doi.org/10.1038/s41598-017-06115-0.

[49] S.S. Hossain, K. Lu, Recent progress of alumina ceramics by direct ink writing: ink design, printing and post-processing, Ceram. Int. 49 (2023) 10199–10212, https://doi.org/10.1016/j.ceramint.2023.01.143.

[50] U. Kalsoom, S. Waheed, B. Paull, Fabrication of humidity sensor using 3D printable polymer composite containing boron-doped diamonds and LiCl, ACS Appl. Mater. Interfaces 12 (2020) 4962–4969, https://doi.org/10.1021/acsami.9b22519.

[51] M. Wu, F. Liu, Y. Lin, M. Wang, S. Zhou, C. Zhang, Y. Mu, G. Han, L. Hao, Parameter optimization via orthogonal experiment to improve accuracy of metakaolin ceramics fabricated by direct ink writing, Chin. J. Mech. Eng.: Additive Manufacturing Frontiers 2 (2023) 100098, https://doi.org/10.1016/j.cjmeam.2023.100098.

[52] K.T. Estelle, B.A. Gozen, Complex ink flow mechanisms in micro-direct-ink-writing and their implications on flow rate control, Addit. Manuf. 59 (2022), https://doi.org/10.1016/j.addma.2022.103183.

[53] S. Ali, A. Hassan, G. Hassan, J. Bae, C.H. Lee, All-printed humidity sensor based on gmethyl-red/methyl-red composite with high sensitivity, Carbon N Y 105 (2016) 23–32, https://doi.org/10.1016/j.carbon.2016.04.013.

[54] C. Cai, W. Zhao, J. Yang, L. Zhang, Sensitive and flexible humidity sensor based on sodium hyaluronate/MWCNTs composite film, Cellulose 28 (2021) 6361–6371, https://doi.org/10.1007/s10570-021-03926-3.

[55] W. Jian, R. Jia, J. Wang, H.X. Zhang, F.Q. Bai, Iron oxides with a reverse spinel structure: impact of active sites on molecule adsorption, Inorg. Chem. Front. 6 (2019) 2810–2816, https://doi.org/10.1039/c9qi00790c.

[56] T. Islam, Z. Uddin, A. Gangopadhyay, Sensors & transducers temperature effect on capacitive humidity sensors and its compensation using artificial, Neural Network. 191 (8) (2015) 126.

[57] T. Dinh, N.-T. Nguyen, D.V. Dao, Thermoelectrical Effect in SiC for High-Temperature MEMS Sensors, SPRINGER BRIEFS IN APPLIED SCIENCES AND TECHNOLOGY, 2018. http://www.springer.com/series/8884.

[58] D.P. Kozlenko, L.S. Dubrovinsky, S.E. Kichanov, E.V. Lukin, V. Cerantola, A. I. Chumakov, B.N. Savenko, Magnetic and electronic properties of magnetite across the high pressure anomaly, Sci. Rep. 9 (2019), https://doi.org/10.1038/s41598-019-41184-3.

[59] E.M. Amin, N. Karmakar, B. Winther-Jensen, Polyvinyl-alcohol (Pva)-based Rf Humidity Sensor in Microwave Frequency, 2013.